Density measurements in shock-compressed aluminium via betatron x-ray radiography

Contact: m.rutherford13@imperial.ac.uk

M. E. Rutherford, D. J. Chapman and D. E. Eakins
Institute of Shock Physics, Blackett Laboratory, Imperial College London, SW7 2BW, UK

J. C. Wood, N. C. Lopes, K. Poder, S. P. D. Mangles and Z. Najmudin
John Adams Institute of Accelerator Science, Blackett Laboratory, Imperial College London, SW7 2BW, UK

Abstract

A GeV level laser wakefield accelerator driven by the Gemini laser was used to produce a bright ($> 10^7$ photons/shot/mm^2 at the detector), hard (18 ± 0.6 keV critical energy) source of betatron x-ray radiation. The betatron pulse was used as an ultrafast, high signal to noise ratio probe of the subsurface physics of a laser driven shock wave in a solid density aluminium target. The target dynamics were imaged as a function of delay in the range $0 - 130$ ns with a spatial resolution of approximately 4 µm, similar to what has been achieved at synchrotron light sources [1–3]. It is shown that quantitative density measurements of the shock-compressed material can be made with this source, and that this source is capable of directly measuring spall fracture at the mesoscale. Spatially-resolved measurements of density in materials under extreme conditions are important for validating equation of state models and understanding the phases of matter inside planets.

Introduction

Shock compression causes a nearly-discontinuous change in thermodynamic conditions within a system, subjecting the shocked material to extremes of pressure (GPa-TPa), temperature (1000's K) and strain-rate (10^5-10^8 s^{-1}). When a shock wave is driven into an ambient sample, the final material state will lie on the locus of all possible shock states known as the principal Hugoniot. If the material is then compressed further from this Hugoniot state, new areas of phase space can be explored and the material is taken to a so-called off-Hugoniot state. These areas of phase space are of significant interest in planetary science, as it is understood that many planetary interiors contain materials at pressures and temperatures that are not accessible from a single shock alone [4]. Shock compression is therefore a powerful tool with which to explore the high pressure-temperate states of matter which are found in planetary cores as well as in the aerospace industry, defence scenarios and nuclear fusion.

Traditionally, the response of solid materials to shock compression has been probed with time-resolved, surface-based diagnostics such as high-speed optical photography, or laser-based velocimetry [5]. While these diagnostics can routinely provide sub-1% precision macroscopic equation of state measurements [6] they do not resolve the sub-surface, microscopic deformation phenomena which ultimately dictate how the sample deforms. In recent years, advances in computational capabilities have made modelling shock-compression at the mesoscale (µm-mm, ns-µs) significantly more accessible, which have begun to provide insight into the relative importance of early-time, mesoscopic processes such as void nucleation or collapse, local phase transitions or instability formation on the macroscopic response of a shocked materials [7, 8]. Therefore, new diagnostics which are capable of making µm-mm, ns-µs resolution, sub-surface measurements of shock-compression are needed to provide experiment insight into mesoscale deformation mechanisms and validate leading computational models.

High-energy radiation is required to penetrate material surfaces and provide information on their internal structure through imaging, scattering or spectroscopic techniques. X-ray radiography is an ideal tool with which to probe sub-surface phenomena non-invasively because it can provide spatially-resolved measurements of interface positions and mass density. Moreover, a number of sub-µs, high-flux x-ray sources are available in-house and at national facilities. While alternative sources of penetrating radiation such as protons (e.g. the 800 MeV P-Rad facility at LANL [9]) have been shown to provide high-fidelity measurements of shock-compression, they are very limited in their availability. Very recently, the use of x-ray sources, including synchrotron radiation [3, 10, 11] and x-ray free electron lasers (XFELs) [12, 13], to make quantitative measurements of mesoscale deformation during shock-compression has been demonstrated. It was previously demonstrated on Gemini, for the first time, that *in-situ* quantitative measurements of shock-compression could be made using betatron x-rays produced by a laser wakefield accelerator (LWFA) [14]. These betatron x-rays are attractive for diagnosing dynamic compression scenarios as they offer simultaneously

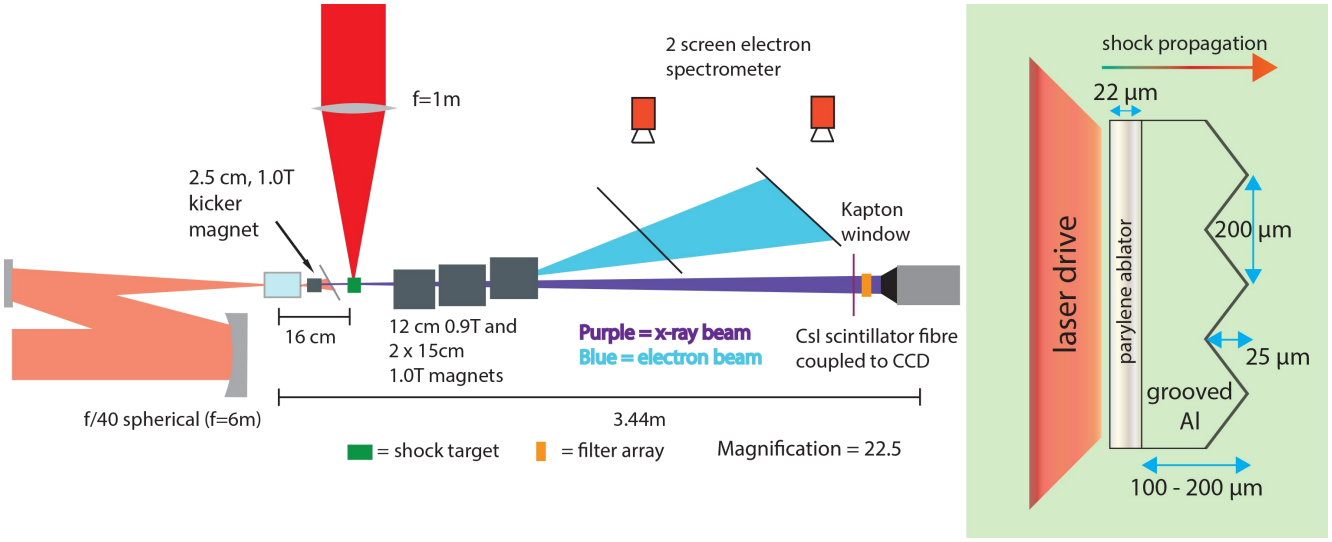

Figure 1: **(Left):** Illustration of the experiment. Shock waves were driven into solid aluminium targets using the north pump beam: 30 J, 40 ns, 1053 nm, 165 µm spot size. During shock propagation, deformation was probed *in-situ* using single-pulse x-ray radiography. X-rays were delivered by a laser wakefield accelerator on the south beamline. Radiographs were recorded on an Andor iKon CCD with a CsI scintillator and a magnification of 22.5. Alongside the shock experiment, a host of typical LWFA diagnostics including electron spectrometers, shadwography and interferometry were fielded to diagnose the laser-plasma interaction. **(Right):** Illustration of the target design.

a short pulse length ($\sim$ 40 fs), polychromatic hard x-ray flux ($\sim$ 10-30 keV), high number of photons ($> 10^9$ per shot) and a small source size ($\sim$ 1 µm) [15]. The scope of quantitative measurements that could be extracted from the radiographs in the previous experiment was, however, limited due to two main reasons:

1. The short duration of the uncompressed North beam, which was used as a shock driver, meant that shocks were not supported for more than 1.5 ns. It was therefore difficult to stroboscopically investigate shock wave propagation and evolution over the 10's ns necessary to see mesoscale phenomena evolve.
2. Several noise sources, such as bremsstrahlung produced by the electron beam striking the shock targets, deteriorated the signal to noise ratio of the radiographs.

This Report describes shock experiments on the Gemini laser. A long pulse laser was fielded to drive supported shocks into aluminium targets for 10's ns. Betatron x-rays were used to record high resolution (40 fs, 4 µm) radiographs during shock propagation, which showed the evolution of a two-wave structure in the sample, and permitted quantitative density measurements.

Method

Figure 1 shows an illustration of the experiment and target design. Shock waves were driven into targets using the north beam. Shock-induced deformation was probed *in-situ* using x-rays produced in a LWFA on the South beamline.

Betatron Radiation

High intensity optical lasers with a normalised vector potential $a_0 \simeq 0.856 \left(I_{18}\lambda_{\mu m}{}^2\right)^{0.5} \gtrsim 1$, where I_{18} is the intensity in units of 10^{18} W/cm^2 and $\lambda_{\mu m}$ is the wavelength in microns, can be used to drive laser wakefield accelerators (LWFA's) [16, 17]. The laser pulse drives a plasma oscillation in its wake, in which the charge separation produces an electron field of order 100 GeV/m. LWFA's have now been use to accelerated electrons beyond 1 GeV in centimetre scale plasmas [18–22]. The electron beam, which typically has some transverse momentum, oscillates due to the transverse focussing forces inside the wakefield and emits radiation: betatron radiation [15, 23]. In the lab frame the frequency of light is boosted by a factor of at least $2\gamma^2$, where γ is the Lorentz factor of the electrons. For GeV electrons this boost takes the photon energy in to the 10's keV region of the spectrum. The wakefield acts in a way analogous to a conventional wiggler insertion device with wiggler parameter $K = \gamma\omega_\beta r_\beta/c$ where r_β is the oscillation radius and the betatron oscillation freqeuncy ω_β is related to the plasma frequency ω_p by $\omega_\beta = \omega_p/\sqrt{2\gamma}$. Reported x-ray source sizes from LWFA's are on the order of a micron [15, 24], making this a promising source for lensless hard x-ray imaging with high resolution with few metre long beamlines. The length of the betatron beam is generally less than one plasma wavelength, meaning its

temporal duration is below 100 fs. Thus it is a suitable source for probing rapidly evolving phenomena.

X-ray source

In the experiment, the LWFA was driven by the Gemini South beam which delivered (11.3 ± 0.6) J of 800 nm light to the target in a pulse with FWHM duration $\sim$ 50 fs. The laser was focussed by an $f/40$ spherical mirror to the entrance of a variable backing pressure, variable length gas cell. After wavefront corrections with a deformable mirror the FWHM spot size was $(58 \pm 1) \times (47 \pm 1)$ µm. This produced a peak intensity of $(6.9 \pm 0.5) \times 10^{18}$ Wcm^{-2} meaning $a_0 = (1.80 \pm 0.06)$. The gas cell was filled with helium to produce a plasma electron number density of $(3.5 - 3.9) \times 10^{18}$ cm^{-3}, and it was held at a length of 16 mm for the optimum imaging conditions.

As Figure 1 shows, after the interaction the residual LWFA drive laser was dumped on a 27 µm thick kapton foil, which acted as a plasma mirror, and a 24 µm aluminium foil. This prevented laser-target interactions from disturbing the shock process. The electron beam was deviated away from the shock target by a 2.5 cm 1.0 T kicker magnet to reduce bremsstrahlung noise in the x-ray image, and then was swept by an arrangement of permanent dipole magnets on to two scintillating Lanex screens to measure its energy spectrum. The mean peak electron energy measured over 42 shots was (940 ± 20) MeV, with 70% of shots having a peak energy between 900 and 1050 MeV.

The betatron x-ray beam was measured at similar parameters to have a beam divergence of $(13 \pm 2) \times (15 \pm 2)$ mrad in the horizontal and vertical directions respectively. The resolution of the imaging system was such that 4 µm features in the target could be resolved, comparable to what has been achieved in shock imaging experiments at conventional 3$^{\text{rd}}$ generation light sources [1–3]. The spectrum of the x-rays was assumed to be an on-axis synchrotron spectrum [25] of the form

$$\frac{d^2I}{dEd\Omega} \propto \gamma^2 \left(\frac{E}{E_c}\right)^2 K_{2/3}^2 \left(E/2E_c\right), \qquad (1)$$

where $K_{2/3}$ is a modified Bessel function of the second kind and the critical energy E_c is given by

$$E_c = \frac{3\hbar}{4c}\gamma^2 {\omega_p}^2 r_\beta. \qquad (2)$$

To estimate the critical energy x-ray images were taken of an array of different metal filters with an x-ray camera, consisting of a caesium iodide (CsI) scintillator fibre-coupled to a CCD camera. An example filter pack image is inset in Fig. 2. The measured transmission of each filter was compared to calculated values for a range of critical energies, and a least squared fitting was done to find the best fit E_c. The mean critical energy over 42 shots was (18.0 ± 0.6) keV. The x-ray camera has been calibrated to allow a conversion from camera counts to energy deposited in the scintillator [26]. Assuming the beam was a 2D gaussian with FWHM widths given by the measured beam divergence, the number of photons in the beam with energy > 1 keV was found to fluctuate between $2.2 - 3.4 \times 10^{10}$. Assuming a 0.8 µm source diameter, inferred from equation 2 and the electron and x-ray spectral measurements, and a 30 fs betatron pulse duration the peak brightness measured on any shot was 2.5×10^{24} photons/s/mm^2/mrad^2/0.1%BW. The number of photons/shot/mm^2 at the centre of the betatron beam on the detector is shown in Fig. 2. Integrated over all energies there was a peak of 1.3×10^7 photons/shot/mm^2 on the detector, equivalent to 2400 photons/pixel for this system.

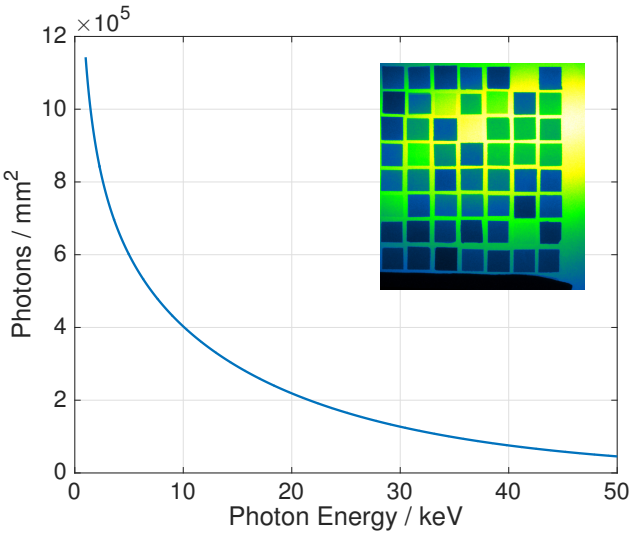

Figure 2: Plot of photons per square mm per shot at the centre of the betatron beam on the detector, as a function of photon energy. Inset (green) is an example image of the filter array.

Target design and scope of work

A target design which allowed for wave propagation and mesoscale phenomena such as fracture or instability growth to be probed with x-ray radiography was desired. Targets were manufactured from aluminium as its attenuation properties are well-suited to transmission radiography experiments with this betatron x-ray source. Targets were 200 µm thick in the x-ray direction and 100-200 µm thick in the laser drive direction. To allow for wave propagation and Richtmyer-Meshkov instability (RMI) growth to be studied, periodic grooves were machined into the rear surfaces of the targets [27–29]. RMI growth occurs when perturbations are amplified upon release of a shock at the rear surface

of a sample, and has been shown to provide one of only a few ways to measure material strength - the resistance to shear stress - at high strain-rates [27, 29]. For the available shock driver in this experiment the target thickness proved to be too thick for RMI growth experiments. However, these thick targets provided an opportunity to study shock compression, re-shock to off-Hugoniot states, release, and subsequent spall fracture.

A 22 µm parylene ablator was deposited onto the front surface of the Al target. The drive laser was incident on the ablator, from left-to-right in Fig. 1, and drove a shock first into the ablator and then into the Al. An ablator was used to mitigate spatial inhomogeneities in the drive laser spot, and to help support the shock stress in the Al for longer [30]. To prevent low-intensity laser energy penetrating the ablator and interacting with the Al target before a shock wave was created the ablator was coated with 100 nm Al.

Shock driver

Many mesoscale shock phenomena of interest evolve over 10's ns. Therefore, a shock driver capable of supporting shocks for this duration was required. A long-duration ($\sim$ 40 ns) shock driver was delivered by introducing a Pockels cell into the Gemini north pump beam. This yielded a pulse with the temporal intensity profile shown in Fig. 3. Preliminary simulations with the radiation-hydrodynamics HYADES code [31] showed that pulse durations of this order with 10's J energy would be sufficient to drive shock stresses of 10's GPa in the Al targets.

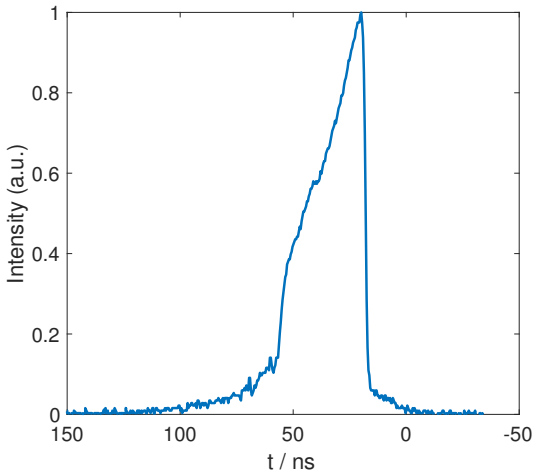

Figure 3: Temporal intensity profile of the North pump beam.

The pulse contained 30 J of energy at a wavelength of 1053 nm, and was focussed to a point just behind the target by the 1 m focal length lens. The spatial profile of the defocussed pulse at the surface of the target was close to a 2D gaussian with FWHM width of 150 µm in x (out of the page in the images) and 180 µm in y (vertical in the images). The peak intensity on the target was approximately 3.5×10^{12} W/cm^2.

Results

A set of radiographs of shock propagation in the aluminium targets were recorded with different delays between the arrival of the shock driver pulse and the betatron pulse at the target. The timing difference was measured from the front of the foot of the pulse ($t = 0$ in Fig. 3), which is shown in Fig. 3. An example radiograph taken at a delay of 30 ns is shown in Fig. 4A.

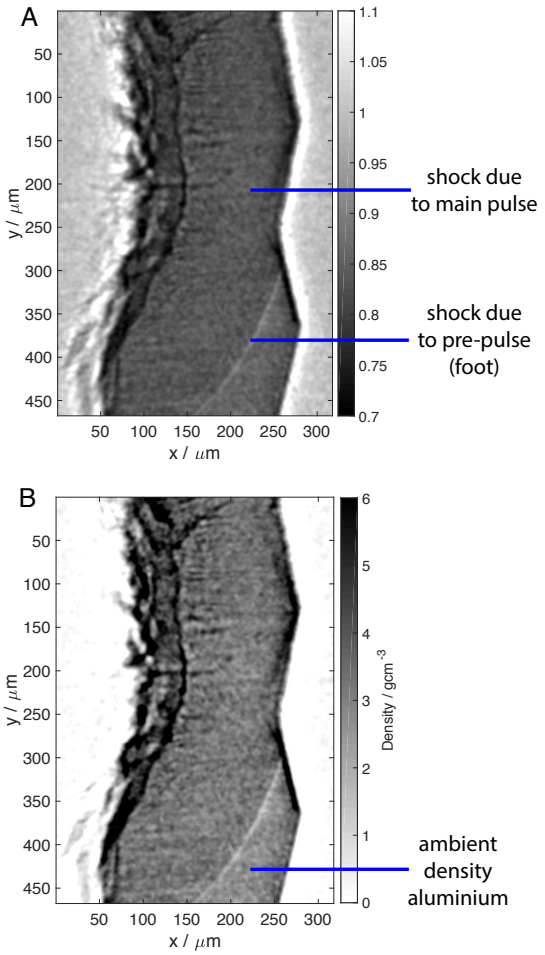

Figure 4: A: Betatron x-ray radiograph of shock propagation in the aluminium target 30 ns after the start of the interaction. B: Density map of the shocked target retrieved assuming a 19.2 keV critical energy synchrotron spectrum.

A number of image corrections were made to the raw data to produce this image. First, dark field and flat

field corrections were performed to remove the dark noise and read noise from the camera, and to correct for the non-uniform response of the scintillator and fibre bundle. To correct for the spatially varying intensity profile of the x-ray beam across the target, an intensity profile was interpolated from surrounding regions of the image. The entire image was divided, pixel by pixel, by this intensity profile to create what was, in effect, a map of x-ray transmission of the target relative to the laser blocking materials and the vacuum window. To remove hard hits from the image, which were likely the result of bremsstrahlung created by the electron beam, the image was selectively median filtered. All pixels with a value > 1.08 times (> 3 standard deviations of photons/pixel) larger than the median of their neighbouring 8 pixels were replaced by the median value of the neighbouring pixels. The image was then smoothed by applying a gaussian blur. The kernel for this had a standard deviation of 2.5 pixels, small compared to the FWHM of the point spread function of the imaging system which was 7-8 pixels.

Figure 4B shows a density map calculated from the x-ray transmission image, assuming that the target remained 200 µm thick throughout the interaction. The transmission R of the target relative to the background (i.e. rest of the x-ray radiograph) is given by

$$R = \frac{\int_0^\infty S(E, E_c)\ T_b(E)\ T_{Al}(E)\ Q(E)\ dE}{\int_0^\infty S(E, E_c)\ T_b(E)\ Q(E)\ dE}. \qquad (3)$$

S is the on-axis synchrotron spectrum from equation 1, normalised such that the integral over all energies is unity, Q is the quantum efficiency of the detector, T_b is the x-ray transmission of the laser block, vacuum window and air in front of the camera and T_{Al} is the transmission of 200 µm aluminium of currently unknown density. The critical energy E_c for the radiograph presented in 4A was estimated from the transmission of the unshocked region of aluminium in the bottom right corner of the target, which had a density of $2.70\,\mathrm{g\,cm^{-3}}$. For this shot $E_c = 19.2\,\mathrm{keV}$. For each pixel in the radiograph, the integral in equation 3 was calculated for a range of trial densities with the best density found by minimising the difference between the calculated and measured transmission.

The radiographs in Fig. 4 show that the temporal foot of the pulse played a significant part in the interaction by driving a two-wave structure into the target. The aluminium was first shocked to a Hugoniot state by the foot, and then re-shocked to an off-Hugoniot state by the trailing high-intensity pulse. The small focus of the laser beam caused approximately spherical, rather than planar, shock waves to propagate into the target. Assuming no change in the x-ray spectrum either side of the first shock front (driven by the foot of the laser drive), the density of material behind the shock ρ_1 was calculated to be $3.07\,\mathrm{g\,cm^{-3}}$, an increase of approximately 14%. An error on ρ_1 was estimated by allowing the critical energy to vary by ±5%, resulting in a value of $\rho_1 = 3.07 \pm 0.16\,\mathrm{g\,cm^{-3}}$.

Simulations of the laser-target interaction were performed in HYADES 1D using a SESAME equation of state for Al. The simulations used the measured temporal profile and a gaussian spatial profile with a FWHM of 165 µm; the mean FWHM measured on the experiment. Figure 5 shows pressure profiles from the HYADES simulation. The experimental radiograph in Fig. 4A was

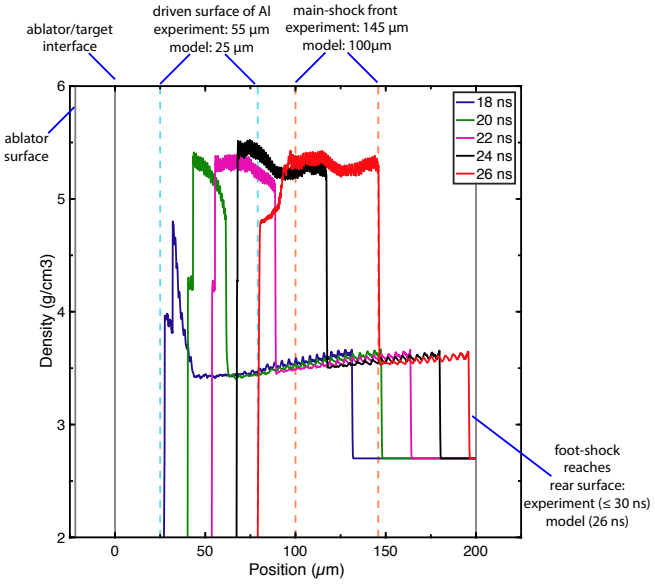

Figure 5: Pressure profiles from a HYADES simulation of the laser-target interaction 18-26 ns after the drive laser interacted with the ablator. Dashed blue and orange lines mark, respectively, the positions of the shocked rear surface and main-shock front in the experiment and model.

recorded at a drive-x-ray delay of 30 ns at which time the foot-shock had reached the rear surface of the target. This position of the foot-shock was reproduced at 26 ns in the simulations, suggesting immediately that the simulations were overestimating the compression of the target. Further discrepancies were seen between the model and experiment. Firstly, the main-shock was observed to trail the foot-shock by approximately 110 µm in experiment. In contrast, the model predicted a separation of 50 µm between these waves. Dashed blue and orange lines mark, respectively, the positions of the shocked rear surface and main-shock front in the experiment and model. The oscillations in the modelled density profiles are numerical artefacts as a result of simulating a discontinuous shock in a meshed simulation. Moreover, the density in the foot-shock region in

the model of $3.55\,\mathrm{g\,cm^{-3}}$ is larger than that measured, $3.07 \pm 0.16\,\mathrm{g\,cm^{-3}}$. These discrepancies were thought to arise, primarily, due to the three-dimensional nature of the experiment, which saw an expanding shock wave enter the target, whereas the model was 1D. The expansion of the shock wave would lead to a slower shock velocity and lower density, as observed. Future work will address this discrepancy by implementing the measured spatial profile into the two-dimensional H2D code, which was recently acquired by CLF.

Figure 6 shows a the temporal evolution of the shock-induced damage in the Al targets over 130 ns recorded across several shots. At 50 ns into the deformation the growth of a spall fracture plane was observed near the rear surface of the sample as a result of interacting release waves driving the sample into a large tensile stress. These radiographs represent some of the first direct measurements of spall fracture at the mesoscale [32] and when combined with the density retrieval method outlined above could lead to measurements of release density and density in the spalled region; parameters useful for equation of state and fracture models, respectively. Reproducing the complex stress states and wave interactions created in these experiments would provide a stringent test of computational models, and suggest that there is rich scope for future experiments to use betatron radiography to study extreme deformation processes at the mesoscale. Moreover, in inertial confinement fusion scenarios the drive laser is shaped in time in order to maximise compression of the target. One method that has been reported to perform well is the use of a high-foot drive, in which the target is initially shocked and then ramp-compressed [33]. The experiment and diagnostic reported here represents one method to directly resolve the mesoscopic deformation of a sample in a drive scenario somewhat like a high-foot implosion. Future work should thus capitalise on the ability to temporally shape the drive laser and the high-spatiotemporal resolution of the x-ray source by digging deeper into the mesocale aspects of structured drives.

Summary and outlook

A series of shock-compression experiments were performed on the Gemini laser. Expanding shock waves were driven into aluminium targets using a long-pulse shock driver. X-rays from a betatron source were used to measure the shock propagation in the targets and, for the first time, retrieve quantitative mass-density values from the radiographs. Significant improvements in shock conditions and radiographic signal-to-noise were achieved in comparison with the previous Gemini experiment. The mass density values measured from the radiographs were lower than those predicted using 1D modelling, a discrepancy thought primarily to be due to the expansion of the shock wave. Future work will address these discrepancies through 2D simulations. Additionally, numerous radiographs of spall fracture were recorded, which clearly observed the coalescence of voids into the spall plane near the rear surface of the sample. The shock radiography method demonstrated in this report is a novel method of recording high SNR, high-spatiotemporal resolution radiographs of shock-compressed samples at the mesoscale and is very promising for future measurements of equation of state and fracture mechanisms under extreme conditions.

Acknowledgements

The authors would like to firstly thank the Gemini and CLF staff for facilitating the experiment. MER, DJC and DEE thank AWE, EPSRC and Imperial College London funding. MER would like to thank John Pasley for access to HYADES and Raoul Trines and Robbie Scott for their assistance and advice. JCW, NCL, KP, SPDM and ZN acknowledge funding from STFC for the support of the John Adams Institute of Accelerator Science by grants ST/J002062/1 and ST/P000835/1.

Bibliography

[1] B. J. Jensen et al., AIP Adv. **2** (2012).
[2] S. N. Luo et al., Rev. Sci. Instrum. **83** (2012).
[3] B. J. Jensen et al., J. Appl. Phys. **118**, 195903 (2015).
[4] M. D. Knudson et al., Phys. Rev. Lett. **108**, 091102 (2012).
[5] L. M. Barker, J. Appl. Phys. **43**, 4669 (1972).
[6] M. D. Knudson and M. P. Desjarlais, Phys. Rev. B **88**, 184107 (2013).
[7] C. W. Barnes, D. J. Funk, M. P. Hockaday, J. L. Sarrao, and M. F. Stevens, The science of dynamic compression at the mesoscale and the Matter-Radiation Interactions in Extremes (MaRIE) project, in *J. Phys.: Conf. Ser.*, page 092001, 2014.
[8] P. A. Bland et al., Nature Communications **5** (2014).
[9] P. A. Rigg et al., Phys. Rev. B **77**, 220101 (2008).
[10] J. A. Hawreliak et al., Sci. Rep. , 1 (2016).
[11] M. E. Rutherford et al., Sci. Rep. (2017).
[12] A. Schropp et al., Sci. Rep. , 1 (2015).
[13] J. Hawreliak, D. Erskine, A. Schropp, E. C. Galtier, and P. Heimann, in *Shock Compression of Condensed Matter 2015*, pages 090006–5, AIP, 2017.
[14] J. C. Wood et al., Ultrafast Imaging of Laser Driven Shocks using Betatron X-rays from a Laser Wakefield Accelerator, in *In preparation*, 2017.
[15] S. Kneip et al., Nature Physics **6**, 980 (2010).
[16] T. Tajima and J. M. Dawson, Phys. Rev. Lett. **4**, 267 (1979).
[17] E. Esarey, C. Schroeder, and W. Leemans, Rev. Mod. Phys. **81**, 1229 (2009).
[18] W. P. Leemans et al., Nat. Phys. **2**, 696 (2006).
[19] S. Kneip et al., Phys. Rev. Lett. **103**, 035002 (2009).
[20] H. T. Kim et al., Phys. Rev. Lett. **111**, 165002 (2013).
[21] X. Wang et al., Nat. Commun. **4** (2013).
[22] W. P. Leemans et al., Phys. Rev. Lett. **113**, 245002 (2014).
[23] A. Rousse et al., Physical Review Letters **93**, 1 (2004).
[24] M. Schnell et al., Phys. Rev. Lett. **108**, 1 (2012).
[25] E. Esarey, B. Shadwick, P. Catravas, and W. Leemans, Phys. Rev. E **65**, 056505 (2002).

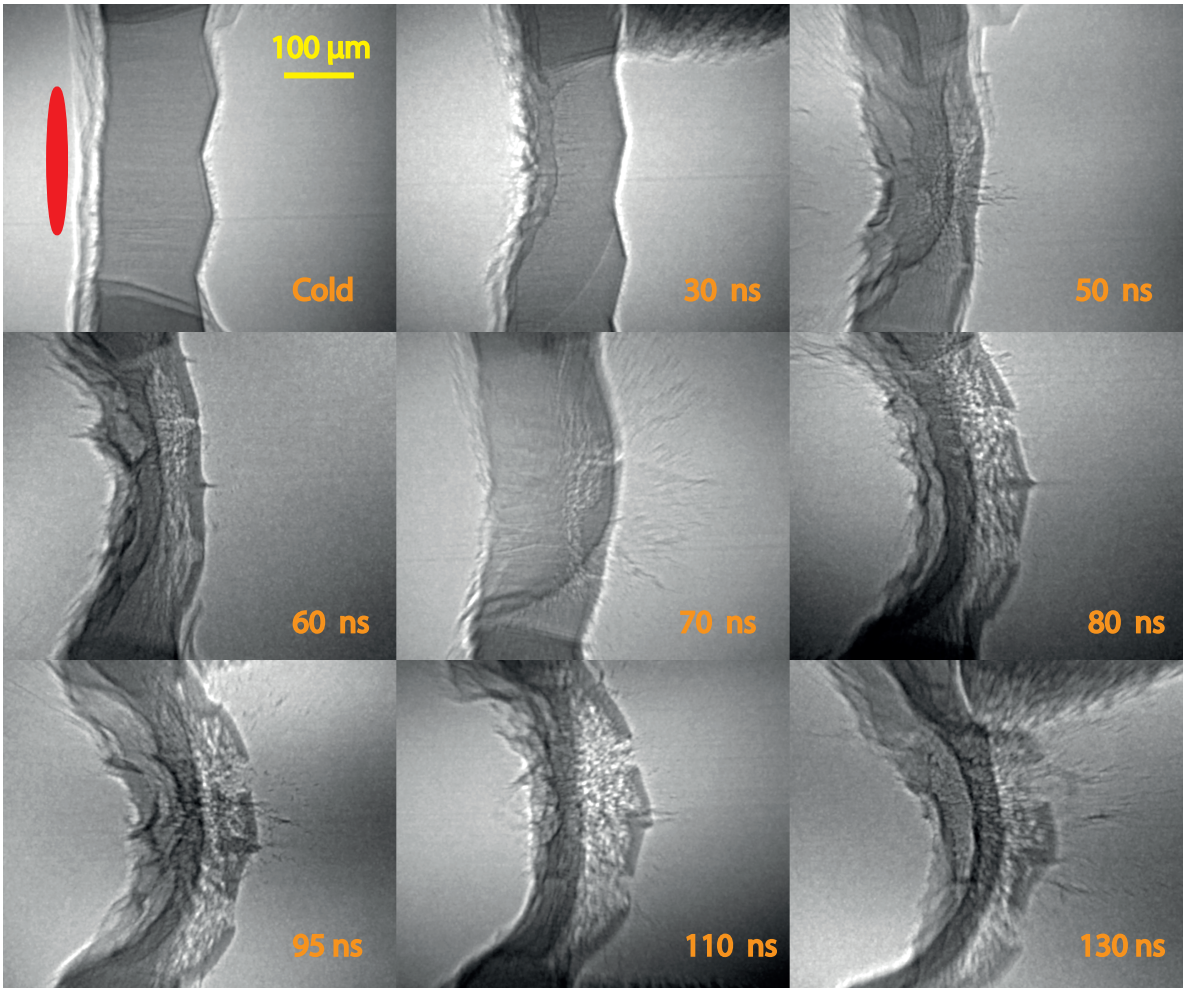

Figure 6: Timing scan of the propagation of the shock, taken over nine shots with different delays. The delay is given by the orange numbers, and cold refers to the unperturbed target before the arrival of the drive laser. The red ellipse shows the approximate FWHM size of the drive laser pulse.

[26] J. C. Wood, R. J. Clarke, S. P. D. Mangles, D. R. Symes, and Z. Najmudin, Calibration of the CLF Andor iKon Indirect Detection X-ray Camera.

[27] G. Dimonte et al., Phys. Rev. Lett. **107**, 264502 (2011).

[28] T. de Rességuier, D. Loison, A. Dragon, and E. Lescoute, Metals **4**, 490 (2014).

[29] W. T. Buttler et al., in *Shock Compression of Condensed Matter 2011*, pages 999–1002, AIP, 2015.

[30] D. C. Swift and R. G. Kraus, Phys. Rev. E **77**, 066402 (2008).

[31] J. T. Larsen and S. M. Lane, J Quant Spectrosc Radiat Transf **51**, 179 (1994).

[32] K. J. Ramos et al., Investigation of Dynamic Material Cracking with In Situ Synchrotron-Based Measurements, in *Dynamic Behavior of Materials, Volume 1*, pages 413–420, Springer International Publishing, Cham, 2013.

[33] N. B. Meezan et al., Plasma Phys. Control. Fusion **59**, 014021 (2016).